



Vertical single or few-layer MoS₂ nanosheets rooting into TiO₂ nanofibers for highly efficient photocatalytic hydrogen evolution

Chengbin Liu^{a,c,*}, Longlu Wang^a, Yanhong Tang^b, Shenglian Luo^{a,c,*}, Yutang Liu^d, Shuqu Zhang^d, Yunxiong Zeng^a, Yuzi Xu^a

^a State Key Laboratory of Chemo/Biosensing and Chemometrics, Hunan University, Changsha 410082, PR China

^b College of Materials Science and Engineering, Hunan University, Changsha 410082, PR China

^c Key Laboratory of Jiangxi Province for Persistent Pollutants Control and Resources Recycle, Nanchang Hangkong University, Nanchang 330063, PR China

^d College of Environmental Science and Engineering, Hunan University, Changsha 410082, PR China

ARTICLE INFO

Article history:

Received 4 June 2014

Received in revised form 21 August 2014

Accepted 30 August 2014

Available online 6 September 2014

Keywords:

Molybdenum disulfide

Vertical standing

Single layer

Photocatalysis

Hydrogen production

ABSTRACT

The catalytic activity of molybdenum sulfide (MoS₂) for hydrogen evolution reaction (HER) strongly depends on the number of exposed active edges of MoS₂ nanosheets. Making single or few-layer MoS₂ nanosheets vertically stand on a substrate is a very effective way to maximally expose the edge sites of MoS₂ nanosheets. Vertically standing single or few-layer MoS₂ nanosheets on porous TiO₂ nanofibers (TiO₂@MoS₂) are successfully prepared via a simple hydrothermal reaction. Due to plenty of pores in the electrospun TiO₂ nanofibers, the MoS₂ nanosheets vertically grow from the inside to the outside, and the growth mode of the MoS₂ nanosheets rooting into the TiO₂ nanofibers endows not only intimate contact between TiO₂ and MoS₂ for fast electrons transfer but also high structural stability of TiO₂@MoS₂ heterostructure. The vertical orientation of MoS₂ nanosheets enables the active edge sites of MoS₂ to be maximally exposed. Without using Pt cocatalyst, the TiO₂@MoS₂ heterostructure achieves high photocatalytic hydrogen production rates of 1.68 or 0.49 mmol h⁻¹ g⁻¹ under UV–vis or visible light illumination, respectively. This high photocatalytic activity arises from the positive synergetic effect between the MoS₂ and TiO₂ components in this novel heterostructure. In addition, the TiO₂@MoS₂ heterostructure exhibits a high durability as evidenced by the invariable hydrogen production rate after continuous illumination over 30 h. The work advances the development of highly efficient molybdenum sulfide-based HER catalysts.

© 2014 Elsevier B.V. All rights reserved.

1. Introduction

Two-dimensional (2D) materials have intrigued not only fundamental science study but also novel materials engineering due to their unique physical and chemical properties [1–3]. It has been proved that the edges of layered materials are the active sites for many important catalytic reactions, such as hydrodesulfurization [4,5], oxygen reduction reactions [6], methane conversion [7], and hydrogen evolution reaction (HER) [8,9]. However, photocatalytic HER by 2D materials has received less attention though electrocatalytic HER has been studied in detail [10–12]. Among the 2D materials, MoS₂ has attracted considerable attention owing to

its extraordinary physical properties and promising applications [13–15], while bulk MoS₂ consisting of face-to-face stacked and weakly interacting MoS₂ layers is a poor HER catalyst [16]. Exposing edges in these cases can boost the catalytic activities. Tremendous efforts have therefore been made to prepare edge-rich MoS₂ materials, including nanosheets [17], nanotubes [18], nanorods [19], and nanofibers [20]. Besides the aspect of active sites, the band gap of MoS₂ is another key consideration for photocatalytic HER. The band gap of MoS₂ increases with decreasing the number of layers due to quantum confinement from the bulk value of 1.2 eV to 1.9 eV for a single monolayer [21], and consequently the conduction band minimum of MoS₂ locates at a more negative potential than the proton reduction potential (H⁺/H₂), which promotes the conduction band electrons to reduce the adsorbed H⁺ and evolve H₂. Recently, Cui's group has prepared MoS₂ films with vertically aligned MoS₂ layers that maximally expose the MoS₂ edges [11]. However, the MoS₂ sheets stacked face-to-face to form a multilayer structure due to the nature of 2D materials. Hence, it is strongly

* Corresponding authors at: State Key Laboratory of Chemo/Biosensing and Chemometrics, Hunan University, Changsha 410082, PR China.

Tel.: +86 731 88823805.

E-mail addresses: chem.cbliu@hnu.edu.cn (C. Liu), slou@hnu.edu.cn (S. Luo).

desired but remains challenging to facilitate prepare MoS₂ catalysts with not only maximally exposed active edge sites but also highly stabilized exfoliated single-/few-layer MoS₂ nanosheets.

In this work, vertically standing single-/few-layer MoS₂ nanosheets on highly porous electrospun TiO₂ nanofibers (TiO₂@MoS₂) were prepared via a simple hydrothermal reaction. The discrete pore distribution on the surface of TiO₂ nanofibers effectively inhibited the growth of MoS₂ crystals along the *c*-axis, resulting in mono or few-layer MoS₂ nanosheets with maximal exposure of MoS₂ edge sites. Furthermore, the MoS₂ nanosheets took root into the TiO₂ nanofibers, enabling the 2D MoS₂ nanosheets to be firmly attached to the TiO₂ nanofibers, which could avoid not only the face-to-face restacking of MoS₂ nanosheets but also the abscission of MoS₂ nanosheets from TiO₂ nanofibers during photocatalysis operation. Additionally, the growth mode of the MoS₂ nanosheets rooting into the TiO₂ nanofibers endows intimate contacts between TiO₂ and MoS₂, favoring effective electron transfer in the TiO₂@MoS₂ heterostructure. As expected, the synthesized TiO₂@MoS₂ heterostructure exhibits highly efficient and stable photocatalytic hydrogen production without requiring the Pt cocatalyst.

2. Experimental

2.1. Chemicals

Poly (vinylpyrrolidone) (PVP, Mw = 1,300,000) was purchased from Alfa Aesar. All other reagents and materials were obtained commercially from the Beijing Chemical Reagent (Beijing, China) and used as received without further purification.

2.2. Synthesis of porous electrospun TiO₂ nanofibers

Typically, 0.45 g of PVP was dissolved in 3 mL ethanol with vigorous stirring for 1 h. 1.5 g of titanium tetraisopropoxide (Ti(O_iPr)₄) was dissolved in a mixture of 3 mL ethanol and 3 mL acetic acid by stirring for 1 h to obtain a homogeneous precursor solution, and then the above PVP solution was added to the homogeneous precursor solution, followed by vigorous stirring for 3 h. The mixed solution was put into a syringe for electrospinning. An electrical potential of 10 kV was applied at an electrode distance of 15 cm. The mixed solution was ejected at a rate of 0.5 mL h⁻¹, resulting in electrospun nanofibers. The as-collected nanofibers were calcined at 450 °C for 2 h in air atmosphere to remove PVP with the formation of TiO₂ crystals. PVP acted as here both linkers between the inorganic precursors to facilitate electrospinning and porogenic agents to obtain porous TiO₂ nanofibers after the PVP removal by a calcination process.

2.3. Preparation of TiO₂@MoS₂ heterostructures

The formation process of TiO₂@MoS₂ heterostructures was described below: typically, 45 mg sodium molybdate (Na₂MoO₄·2H₂O) and 90 mg thioacetamide (C₂H₅NS) were dissolved in 20 mL deionized water to form a transparent solution. Then 20 mg calcined TiO₂ nanofibers were added into the above solution and stirred to get a suspension. The suspension was transferred to a Teflon-lined stainless steel autoclave and then heated in an electric oven at 220 °C for 24 h. The solid product was dried at 80 °C for 12 h to obtain TiO₂@MoS₂ heterostructures (containing 60 wt% of MoS₂). The content of MoS₂ in TiO₂@MoS₂ could be tuned by adjusting the amount of Na₂MoO₄·2H₂O and C₂H₅NS precursors, and only the optimized TiO₂@MoS₂ sample containing 60 wt% of MoS₂ was used for analysis in detail unless

otherwise stated. For comparison, pure MoS₂ nanosheets were prepared under the same conditions without TiO₂ nanofibers.

2.4. Characterization

The morphologies and microstructures of the samples were characterized using an S-4800 field emission scanning electron microscope (FESEM, Hitachi, Japan) and a transmission electron microscope (TEM, JEOL JEM-2100F). The EDS mapping images were captured on a Tecnai G2 F20 S-TWIN atomic resolution analytical microscope. The crystal phases of the samples were collected on an X-ray diffractometer with Cu-Kα radiation (XRD, M21X, MAC Science Ltd., Japan). The binding energies of S, Mo, and O of the heterostructures were determined by X-ray photoelectron spectroscopy (XPS, K-Alpha 1063, Thermo Fisher Scientific, England) using an Al-Kα X-ray source. The UV–vis diffuse reflectance spectra (DRS) were performed on a UV–vis spectrophotometer (Cary 300, USA) with an integrating sphere. The photoluminescence (PL) spectra were recorded with Hitachi F-2500 fluorescence spectrophotometer at an excitation wavelength of 514 nm. The BET specific surface areas were measured on Belsorp-Mini II analyser (Japan). The thermogravimetric analysis (TGA) curves were collected with TG/DTA7300 (Germany) from room temperature to 800 °C with a heating rate of 10 °C/min and an O₂ flow rate of 50 mL min⁻¹.

2.5. Photoelectrochemical measurements

The photoelectrochemical measurements of the samples were carried out on a three-electrode electrochemical workstation (CHI 600D, Chenhua, China) equipped with an FTO electrode deposited with the TiO₂@MoS₂ heterostructure as the working electrode, a platinum foil as the counter electrode, and a saturated calomel electrode (SCE) as the reference electrode. All the samples were analyzed in 0.35 M/0.25 M Na₂S–Na₂SO₃ aqueous solution without bias potential at room temperature. A 300 W xenon arc lamp with light wavelength range of 320–780 nm (Perfectlight, PLS-SXE 300C, Beijing, China) was used as light source with 100 mW/cm² incident light intensity.

2.6. Photocatalytic hydrogen production tests

The photocatalytic hydrogen evolution experiments were performed in a 100 mL sealed quartz flask at ambient temperature and atmospheric pressure. A 300 W xenon arc lamp with lighting wavelength range of 320–780 nm (Perfectlight, PLS-SXE 300C, Beijing, China) was used as light source to trigger the photocatalytic reaction. The lamp was positioned 10 cm away from the reactor where the focused intensity on the flask was 168 mW cm⁻². In a typical photocatalytic experiment, 4 mg of photocatalysts were dispersed in an 80 mL mixed aqueous solution containing 0.35 M Na₂S and 0.25 M Na₂SO₃. Before irradiation, the system was bubbled with nitrogen for 30 min to remove the air ensuring the reaction system in an inertial condition. The hydrogen was analyzed by a gas chromatography (GC2010, Shimadzu) equipped with a thermal conductive detector (TCD) and a 5 A molecular sieve column, using nitrogen as the carrier gas.

3. Results and discussion

Fig. 1a shows the field emission scanning electron microscope (FESEM) image of the calcined electrospun TiO₂ nanofibers with a diameter of ca. 110 nm. The surface of the TiO₂ nanofibers composed of TiO₂ particles is highly rough and porous due to the removal of PVP porogenic agents by calcination. The abundant defects easily interact with metallic precursors [22], and will act

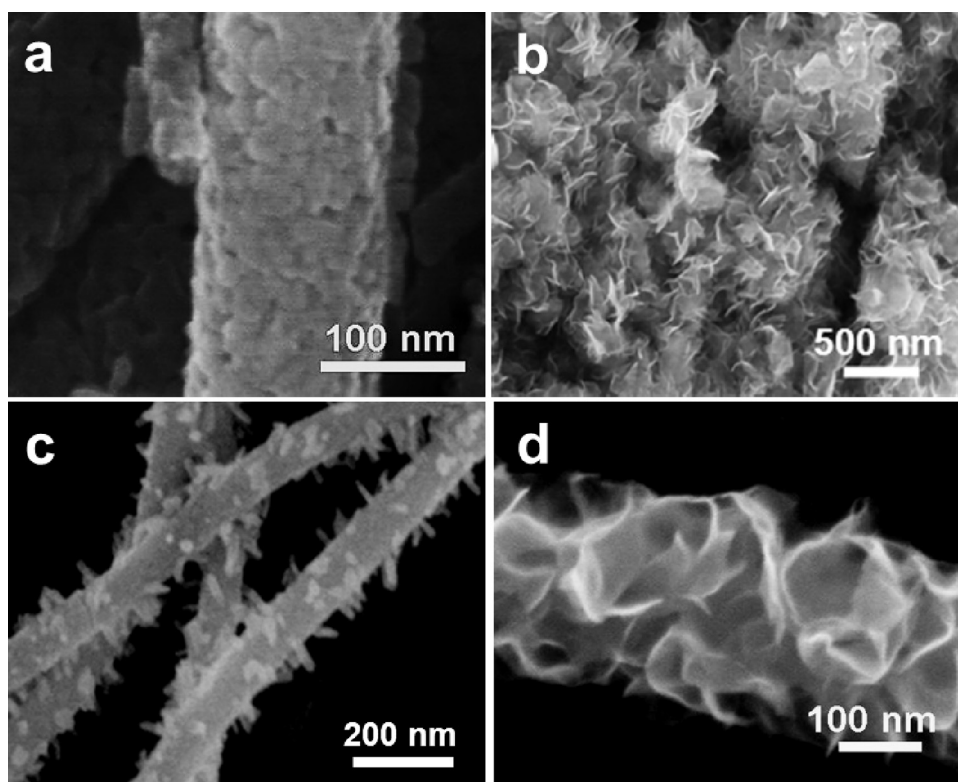
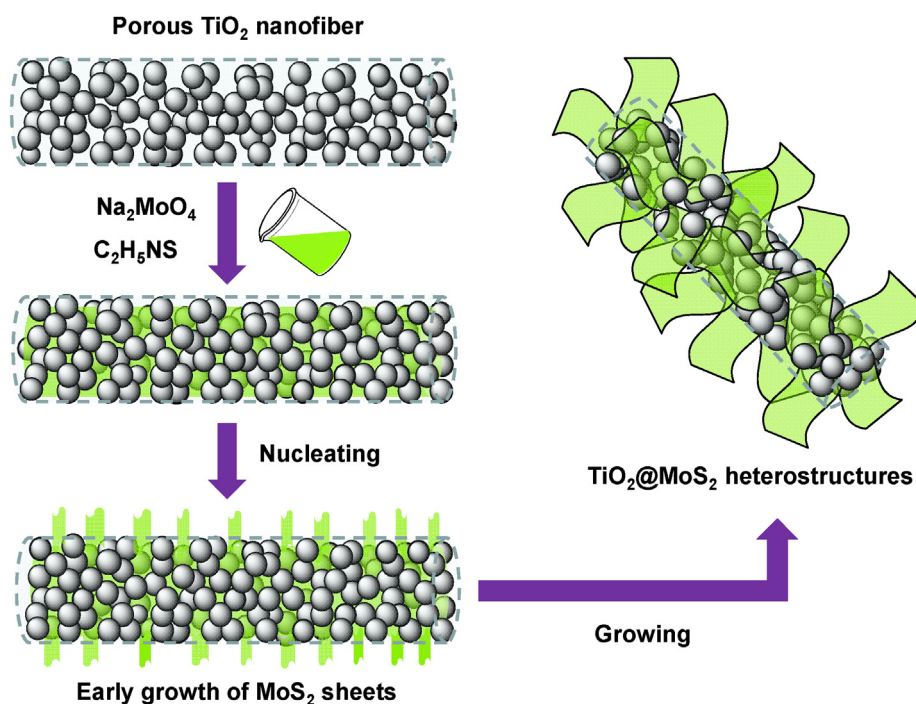


Fig. 1. FESEM images of (a) TiO₂ nanofibers, (b) pure MoS₂ nanosheets, (c) TiO₂@MoS₂ heterostructures prepared via 12-hour reaction, and (d) TiO₂@MoS₂ heterostructure prepared via 24-h reaction.

as nucleation centers for the growth of MoS₂ nanosheets. Fig. 1b exhibits that without using the TiO₂ nanofibers as growth templates, the MoS₂ nanosheets are clustered to form micron-sized agglomerates. Fig. 1c shows the early growth stage of MoS₂ on the TiO₂ nanofibers in the first 12 h, demonstrating small bamboo shoot-like MoS₂ sheets grown perpendicularly onto the surfaces of

TiO₂ nanofibers. Due to plenty of pores in the TiO₂ nanofibers, the precursors of MoS₂ (sodium molybdate and thioacetamide) penetrated into the pores in TiO₂ nanofibers to nucleate MoS₂, and then the MoS₂ embryos grew from the inside to the outside, forming the vertical orientation. This means that: (1) the MoS₂ sheets are deeply rooted in the TiO₂ nanofibers, enabling a high structural stability



Scheme 1. Schematic illustration for the nucleation and growth of MoS₂ nanosheets.

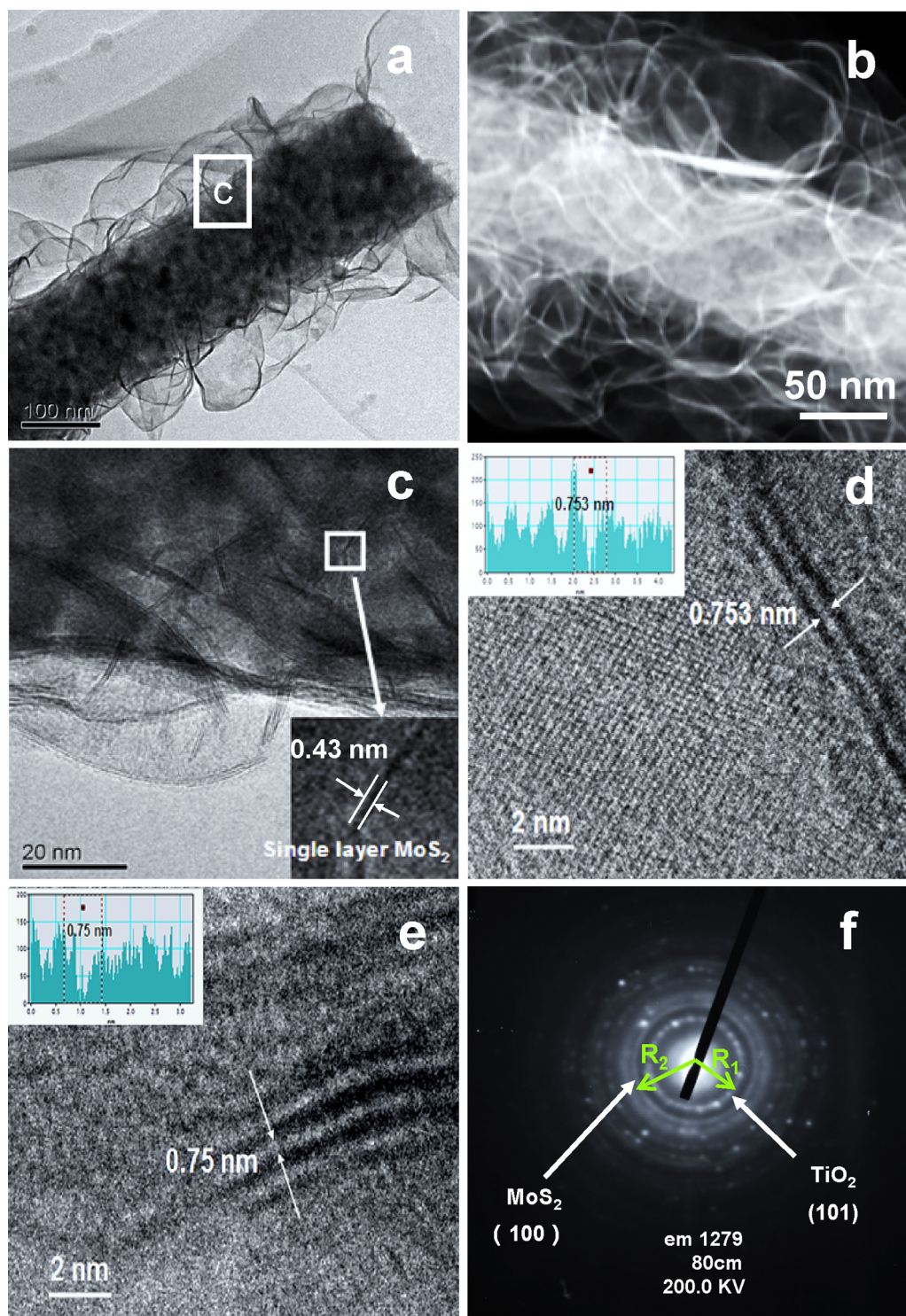


Fig. 2. (a) TEM image of TiO₂@MoS₂ hierostructures, (b) dark field FESEM-STEM image of TiO₂@MoS₂ hierostructures, (c) top-view HRTEM image of designated square parts in (a), (d and e) HRTEM images of (c), and (f) SAED pattern of TiO₂@MoS₂ heterostructures.

of the TiO₂@MoS₂ heterostructure, (2) the perpendicular growth behavior of MoS₂ sheets facilitates the exposure of MoS₂ edge sites, and (3) the MoS₂ sheets growing discretely and disorderly along the axes of TiO₂ nanofibers can not face-to-face restack to form regular multilayers. As revealed in Fig. 1d, with the reaction time extending to 24 hours, the vertical MoS₂ embryos grew larger into staggered MoS₂ sheets, expanding the diameter from 110 nm of the bare TiO₂ nanofiber to about 300 nm of the coaxial TiO₂@MoS₂

heterostructure nanofiber. The noticeable distortion of the MoS₂ sheets helps to decrease their high surface energy to make the MoS₂ stable as independent ultrathin nanosheet units. The nucleation and growth of the MoS₂ sheets with the TiO₂ nanofibers as templates is illustrated in Scheme 1.

Fig. 2a and b shows the transmission electron microscope (TEM) and dark field FESEM-STEM images of the TiO₂@MoS₂ heterostructures, respectively. It is clearly revealed that the MoS₂ sheets

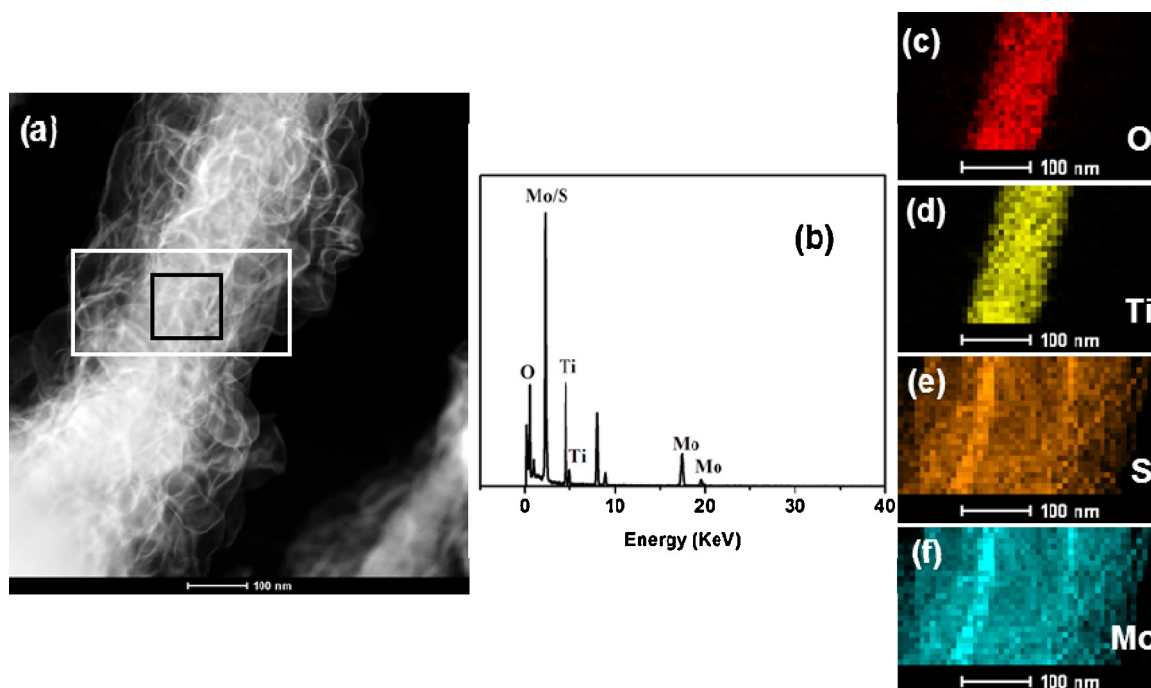


Fig. 3. (a) High magnification dark field FESEM-STEM image of $\text{TiO}_2@\text{MoS}_2$ heterostructures, (b) EDX spectrum of the indicated selected area by the black box in (a), and (c–f) elemental mappings of the selected area by white box in (a).

with a lateral size of about 100 nm vertically stand on the surface of TiO_2 fibers. The MoS_2 sheets are transparent, flexible, and curly, indicative of their ultrathin 2D nature. The freely suspended MoS_2 nanosheets exhibit random elastic deformations and distortion edges which favor the stability of 2D materials [23,24]. Such a morphology is ideal for HER as the vertical orientation of the MoS_2 nanosheets and the resultant open structure can provide high density of active sites [15]. The top-view high resolution TEM (HRTEM) image of $\text{TiO}_2@\text{MoS}_2$ shows that the layer number of the MoS_2 nanosheets deposited on TiO_2 nanofiber is about 1–4 (Fig. 2c). The thickness of a single MoS_2 sheet is 0.43 nm (Inset in Fig. 2c), agreeing with the spacing between two S layers (sandwiching the Mo layer) as derived from bulk data (JCPDS 37-1492). Fig. 2d and e discloses that the spacing of neighboring sheets in the few-layer MoS_2 is about 0.75 nm, larger than 0.61 nm of interlayer spacing in bulk MoS_2 [25]. This means that the individual sheets in the few-layer structure keep independent character, due to the fact that the MoS_2 sheets nucleated and grown at different pore sites along the axes of TiO_2 nanofibers are discrete (as shown in Fig. 1c) and thus the restacking of MoS_2 sheets into regular multilayers can be suppressed. It can be reasonably inferred that the so-called few-layer structure is probably from the imaging overlap of several single-layer MoS_2 sheet edges. Fig. 2f shows the selected area electron diffraction (SAED) where R_1 and R_2 are 5.72 and 7.43 mm, respectively. According to Bragg equation, the corresponding calculated d_1 and d_2 are 3.511 and 2.704 Å ($d_{\text{XRD}} = 3.533$ Å for $\text{TiO}_2(101)$ and $d_{\text{XRD}} = 2.713$ Å for $\text{MoS}_2(100)$ from Fig. 4), respectively. The result confirms the existence of TiO_2 and MoS_2 crystal phases in the $\text{TiO}_2@\text{MoS}_2$ heterostructures.

The energy dispersive X-ray spectrometry (EDX) analysis of the selected area by a black box in Fig. 3a evidences the existence of O, Ti, S and Mo in $\text{TiO}_2@\text{MoS}_2$ heterostructures (Fig. 3b). The EDX elemental mappings show that O dovetails well with Ti while S dovetails well with Mo (Fig. 3c–f), and the mapping width of S (or Mo) is three times larger than that of O (or Ti), consistent with the core (TiO_2 nanofiber) and shell (MoS_2 nanosheets) hierarchical structure. The uniform color and luster of S or Mo mapping means homogeneous dispersion of MoS_2 nanosheets.

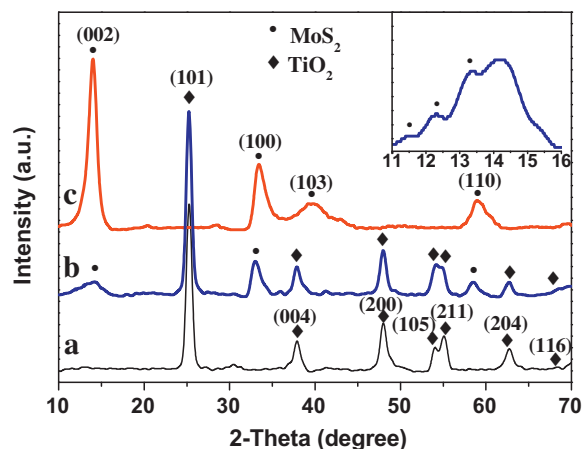


Fig. 4. XRD patterns of (a) pure TiO_2 nanofibers, (b) $\text{TiO}_2@\text{MoS}_2$ heterostructures, and (c) pure MoS_2 nanosheets. Inset is the magnified pattern of the corresponding part of curve (b).

The X-ray diffraction (XRD) patterns of the samples are shown in Fig. 4. The TiO_2 in the samples (Fig. 4a and b) shows standard peaks of the anatase phase (JCPDS 21-1272). The XRD pattern of MoS_2 nanosheets (Fig. 4c) shows the characteristic diffraction peaks at 14° , 33° , 39° and 59° unambiguously assigned to the (002), (100), (103), and (110) planes of MoS_2 ($a=b=0.316$ nm, $c=1.230$ nm, JCPDS 37-1492), respectively. It is found that the (002) peak of MoS_2 nanosheets, which is attributed to the periodicity in c-axis of MoS_2 plane [26], is very weak in $\text{TiO}_2@\text{MoS}_2$ (Fig. 4b) compared to the pure MoS_2 , indicating that the c-axis stacking of MoS_2 sheets occurring in pure MoS_2 is effectively inhibited in $\text{TiO}_2@\text{MoS}_2$. Furthermore, three new peaks emerge at the low-angle region in curve b (see magnified pattern as the inset curve in Fig. 4) for $\text{TiO}_2@\text{MoS}_2$, corresponding to the enlarged interlayer spacings of 6.65, 6.78, and 8.08 Å, respectively. The spacing change hints the formation of a new lamellar structure with increased interlayer spacing compared with 6.15 Å in pristine 2H- MoS_2 (JCPDS 73-1508). This again

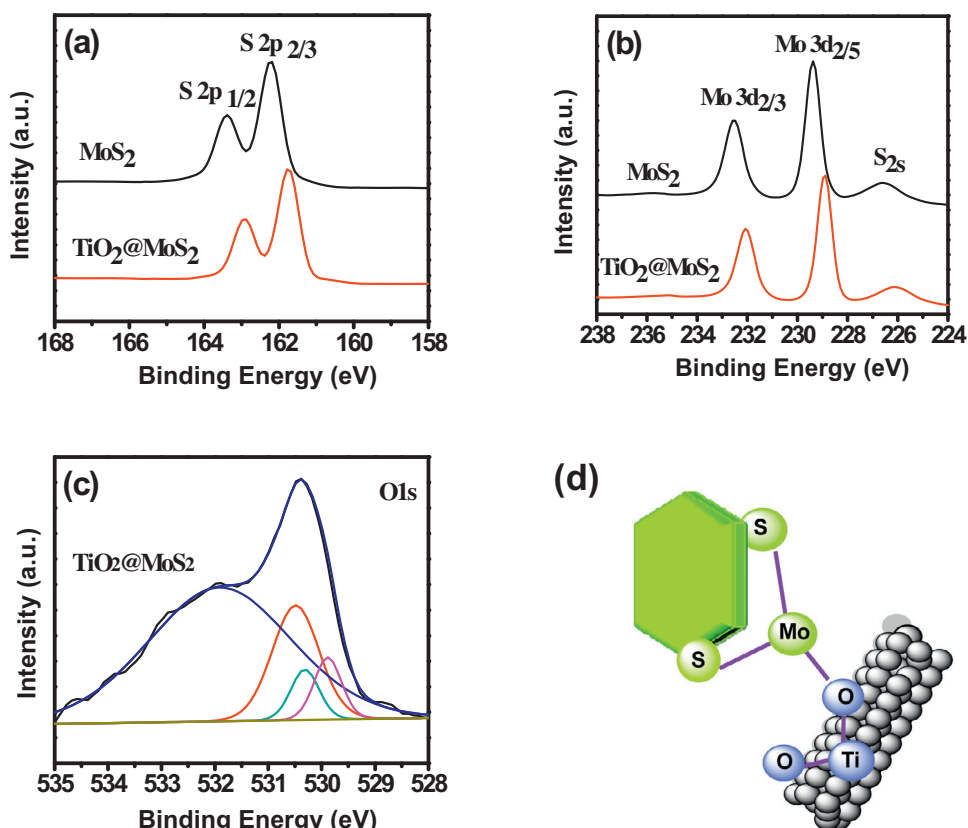


Fig. 5. XPS spectra of pure MoS₂ and TiO₂@MoS₂ heterostructures: (a) S2p peaks of pure MoS₂ and TiO₂@MoS₂, (b) Mo3d peaks of pure MoS₂ and TiO₂@MoS₂, and (c) O1s of TiO₂@MoS₂. (d) The interaction between TiO₂ and MoS₂.

demonstrates that the TiO₂ nanofibers inhibit the growth of MoS₂ sheets along *c*-axis.

The X-ray photoelectron spectroscopy (XPS) analysis was employed to determine the chemical composition and bonding configuration of the as-fabricated products, and the XPS results are shown in Fig. 5a–c. The binding energies of S 2p_{1/2}, S 2p_{3/2}, Mo 3d_{3/2} and Mo 3d_{5/2} peaks in the pure MoS₂ locate at 163.3, 162.3, 232.5 and 229.3 eV, respectively. After MoS₂ nanosheets growing onto the TiO₂ nanofibers, S 2p_{1/2}, S 2p_{3/2}, Mo 3d_{3/2} and Mo 3d_{5/2} peaks shift to 162.9, 161.9, 232 and 228.8 eV, respectively, lower than the corresponding values of pure MoS₂. The binding energy shifts mean electronic interaction between MoS₂ and TiO₂ [27]. As shown in Fig. 5c, besides the O 1s peaks at 529.8 eV attributed to the Ti–O–Ti bond, 532.0 eV attributed to adsorbed water, and 530.5 eV attributed to surface hydroxyl group (Ti–O–H), the O 1s peak at around 530.3 eV is observed, which might be ascribed to the formation of the Ti–O–Mo bonds between MoS₂ and TiO₂ (illustrated as in Fig. 5d) [27].

Table 1 lists the BET data of the prepared materials, and among them TiO₂ nanofibers show the largest specific surface area (52 m²/g) due to its highly porous structure. When the MoS₂ nanosheets took root into the TiO₂ nanofibers, the pores in TiO₂ nanofibers were occupied with MoS₂ nanosheets, making the specific surface area reduce to 27 m²/g. Nevertheless, the TiO₂@MoS₂

hierarchical structure with puffy and loose MoS₂ sheets still shows the specific surface area larger than the pure MoS₂ sheets consisting of densely clustered nanosheets (18 m²/g). A higher specific surface area of photocatalysts can supply more adsorption and reactive sites, contributing to enhancing photocatalytic performance.

The nitrogen adsorption–desorption isotherms and Barrett–Joyner–Halenda (BJH) pore-size distribution plots of the TiO₂ nanofibers, TiO₂@MoS₂ heterostructures and pure MoS₂ nanosheets were used to further study their microstructures (Fig. 6). As shown in Fig. 6a, the isotherm curve of TiO₂ nanofibers exhibits typical adsorption–desorption behavior, suggesting the existence of pores. In contrast, those of pure MoS₂ nanosheets and TiO₂@MoS₂ heterostructures show wholly reversible feature, indicating the absence of pores in pure MoS₂ nanosheets and TiO₂@MoS₂ heterostructures. Additionally, the corresponding BJH pore-size distribution plots also clearly show that the pores from TiO₂ nanofibers disappear in TiO₂@MoS₂ heterostructures, due to the occupation of MoS₂ nanosheets (Fig. 6b).

All above results confirm that the pores in TiO₂ nanofibers play a crucial role in growing vertical ultrathin MoS₂ nanosheets with high structural stability, and the growth mode of MoS₂ sheets from the inside to the outside at discrete sites (pores) along the axes of TiO₂ nanofibers successfully suppresses the restacking of MoS₂ sheets into multilayers, as illustrated in Scheme 1.

Thermogravimetric analysis (TGA) was employed to determine the amount of MoS₂ in TiO₂@MoS₂ heterostructures and check the thermal stability of TiO₂@MoS₂ heterostructures. As shown in Fig. 7, the TiO₂ nanofibers demonstrate a slight weight loss about 1.56% resulting from the dehydroxylation of TiO₂ nanofibers, while both pure MoS₂ and TiO₂@MoS₂ have a distinct weight loss in the range of 300–500 °C, which is ascribed to weight losses along with the transformation of the host MoS₂ into MoO₃ [28].

Table 1
BET data of the materials.

Materials	BET surface area (m ² /g)
TiO ₂ nanofibers	52
TiO ₂ @MoS ₂ heterostructures	27
Pure MoS ₂ nanosheets	18

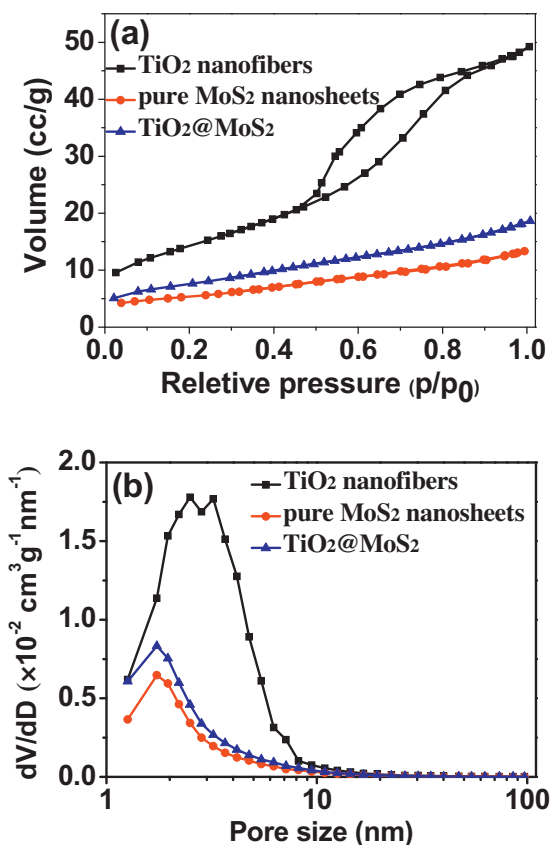


Fig. 6. (a) N₂ adsorption/desorption isotherm curves and (b) BJH pore size distribution of TiO₂ nanofibers, pure MoS₂ nanosheets and TiO₂@MoS₂ heterostructures.

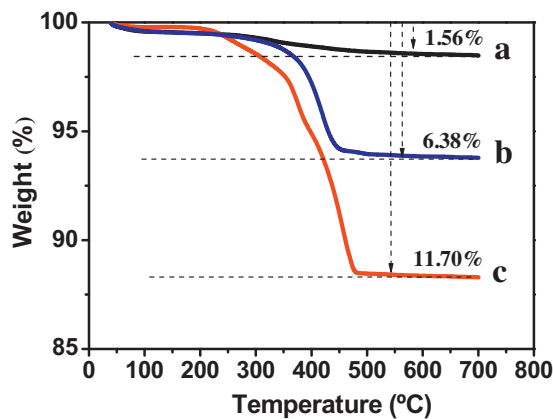


Fig. 7. TGA curves of (a) TiO₂ nanofibers, (b) TiO₂@MoS₂ and (c) pure MoS₂.

So, the approximate amount of MoS₂ can be calculated from TGA analysis by assuming that the remaining product after the TGA measurement is pure MoO₃ for MoS₂ and TiO₂@MoO₃ for TiO₂@MoS₂. MoS₂ is converted into MoO₃ with weight loss about 10% in theory that is basically consistent with 11.7% in our experiment. A weight loss percentage of approximately 6.38% can be seen for TiO₂@MoS₂ heterostructures, and therefore the calculated MoS₂ content in the initial TiO₂@MoS₂ heterostructures is about 60%, with the rest being the TiO₂ nanofiber backbone. It should reinforce the point that the tested MoS₂ content in TiO₂@MoS₂ heterostructures is well consistent with the feed ratio (sodium molybdate-thioacetamide/TiO₂ nanofibers) during the preparation of TiO₂@MoS₂ heterostructures, meaning that the MoS₂ content in TiO₂@MoS₂ heterostructures can be easily regulated by

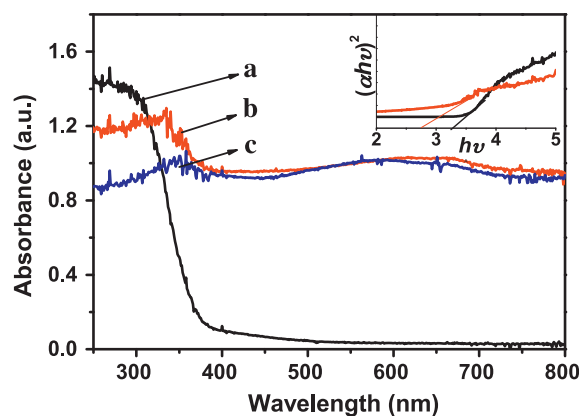


Fig. 8. UV-vis absorption spectra of (a) TiO₂ nanofibers, (b) TiO₂@MoS₂ heterostructures, and (c) pure MoS₂ nanosheets. Inset is the corresponding Kubelka-Munk transformed reflectance spectra to determine the bandgap values for the TiO₂ and TiO₂@MoS₂ heterostructures.

changing the raw material ratio. In addition, pure MoS₂ starts weight loss at 250 °C while TiO₂@MoS₂ heterostructures starts weight loss at 350 °C, implying the better chemical stability of MoS₂ in TiO₂@MoS₂ heterostructures.

There is a great need for structuring photocatalysts to optimize the absorption properties related to bandgap, size, and/or band position [23]. UV-vis absorption spectrum can be used to evaluate bandgaps of semiconductors. As shown in Fig. 8, the pure TiO₂ nanofibers only exhibit the fundamental absorption band in UV light region while both pure MoS₂ and TiO₂@MoS₂ show significantly increased absorption in visible light region. The bandgaps of the photocatalysts can be calculated using the following formula:

$$\alpha = A(h\nu - E_g)^{n/2} / h\nu$$

where α is the absorption coefficient, A is a constant, h is the Planck's constant, E_g is band energy, ν is the frequency of the incident light, and n is equal to 1 for the direct transition. The corresponding Kubelka-Munk transformed reflectance spectra are shown as the inset curve in Fig. 8 where the slopes of the tangents on horizontal axis are bandgap energies. The calculated bandgap energy for TiO₂ nanofibers is 3.15 eV (corresponding to the absorption edge of 400 nm), consistent with the anatase phase of TiO₂, while the narrower bandgap energy of approximately 2.75 eV (corresponding to the absorption edge of 450 nm) for the TiO₂@MoS₂ photocatalyst is very suitable for photocatalytic HER at a reasonable rate [29,30].

It has been proved that MoS₂ photoluminescence (PL) increases with decreasing layer number [31], and due to the indirect-to-direct bandgap transition on going from a bulk to a monolayer arising from quantum confinement effects [21,26], the luminescence is absent in bulk MoS₂ while the strongest from a MoS₂ monolayer. The PL spectra of MoS₂ and TiO₂@MoS₂ were measured using fluorescence spectroscopy at an excitation wavelength of 514 nm only to excite MoS₂ illumination without the interference of TiO₂ (Fig. 9). A broad peak centered at 626 nm (1.98 eV) and a shoulder at 645 nm (1.92 eV) are observed on both MoS₂ and TiO₂@MoS₂ heterostructures. The band gap energies above 1.9 eV confirm the existence of monolayer MoS₂ sheets [21,32]. The PL intensity of the TiO₂@MoS₂ heterostructure is much stronger than that of MoS₂, suggesting much higher degree exfoliation of MoS₂ in the former than in the latter. The photocurrent tests can be used to evaluate the ability of producing charge carriers and the separation of photogenerated electrons. As shown in Fig. 9B, TiO₂@MoS₂ heterostructures show much stronger photocurrent intensity than MoS₂ and TiO₂ nanofibers, meaning stronger ability of producing charge carriers and more separated electrons.

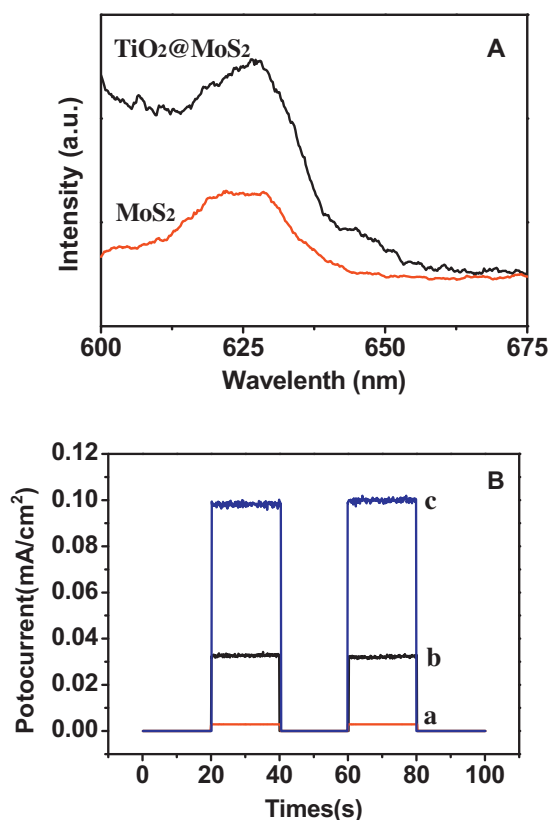


Fig. 9. (A) Photoluminescence spectra of MoS₂ and TiO₂@MoS₂ heterostructures. (B) Photocurrent response of (a) MoS₂, (b) TiO₂ nanofibers, and (c) TiO₂@MoS₂ heterostructures.

Although TiO₂@MoS₂ shows stronger PL intensity with higher recombination of electron–hole pairs, the actual photocatalytic HER is performed in the presence of electron donors where the photogenerated electrons are not involved in recombination but transferred to protons for producing hydrogen. So, TiO₂@MoS₂ is expected to exhibit superior photocatalytic HER.

Fig. 10 presents a comparison of the photocatalytic H₂ production activities of pure TiO₂ nanofibers, TiO₂@MoS₂ (40, 50, 60, and 70 wt% of MoS₂), pure MoS₂ nanosheets, and the physical mixture of TiO₂ nanofibers and MoS₂ nanosheets (TiO₂ + MoS₂ with a weight ratio of 4:6) under UV–vis light irradiation ($\lambda > 320$ nm) (Fig. 10a) or visible light irradiation ($\lambda > 420$ nm) (Fig. 10b) in a mixed aqueous solution containing 0.35 M Na₂S and 0.25 M Na₂SO₃ as sacrificial agents. The pure TiO₂ nanofibers show a poor photocatalytic hydrogen evolution activity although it can absorb UV light, whereas the TiO₂@MoS₂ heterostructures exhibit much higher photocatalytic hydrogen production activities. It is clear that the content of MoS₂ nanosheets has a significant influence on the photocatalytic hydrogen production activity of TiO₂@MoS₂ catalyst. The optimal loading of MoS₂ in TiO₂@MoS₂ is 60 wt%, with the hydrogen production rates as high as 1.68 or 0.49 mmol h^{−1} g^{−1} under UV–vis or visible light illumination, respectively. In contrast, lower loading of MoS₂ (40 or 50 wt%) leads to the insufficient visible light absorption and less active sites, while excessive loading of MoS₂ (70 wt%) may block photogenerated electrons transfer and reduce active site exposure due to highly overlapping each other. The pure MoS₂ nanosheets exhibit lower hydrogen production rate than TiO₂@MoS₂, hinting the beneficial synergetic effect from the TiO₂@MoS₂ heterostructure [33]. In addition, the simple mechanical mixing of TiO₂ nanofibers and MoS₂ nanosheets shows low hydrogen production rates due to the poor interfacial contacts between MoS₂ sheets and TiO₂ nanofibers which extremely inhibit electron transfer.

A tentative mechanism is proposed for the high H₂ production activity of the TiO₂@MoS₂ heterostructures (Scheme 2) [34]. Under

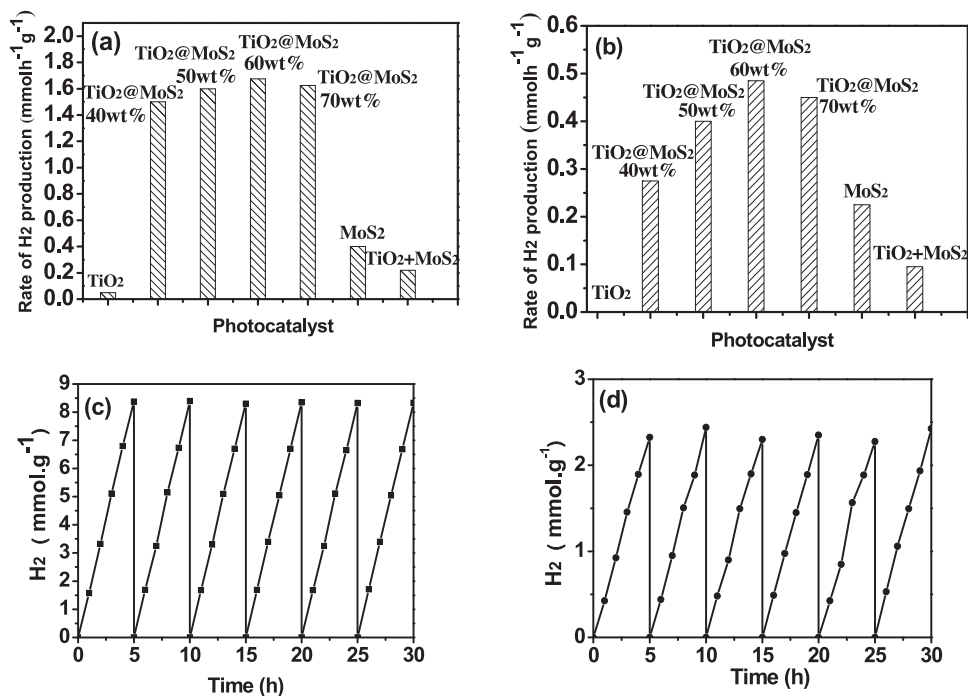
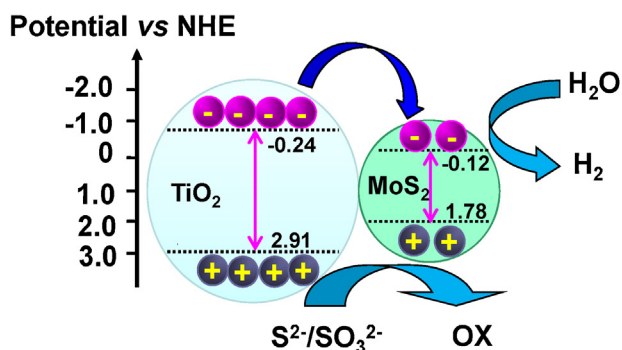


Fig. 10. Comparison of the photocatalytic hydrogen production activities of pure TiO₂ nanofibers, TiO₂@MoS₂ (40, 50, 60, and 70 wt% of MoS₂), pure MoS₂ nanosheets, and the physical mixture of 40 wt% TiO₂ nanofibers and 60 wt% MoS₂ nanosheets under the illumination with the same lighting source (a) ($\lambda > 320$ nm) and (b) ($\lambda > 420$ nm) in the mixed aqueous solution containing 0.35 M Na₂S and 0.25 M Na₂SO₃ as sacrificial agents. Cyclic H₂-evolution curves for TiO₂@MoS₂ (60 wt% of MoS₂) (c) ($\lambda > 320$ nm) and (d) ($\lambda > 420$ nm).



Scheme 2. Schematic illustration of the energy band structure of the $\text{TiO}_2@\text{MoS}_2$ heterostructure and the proposed charge transfer mechanism.

UV illumination, the valence band (VB) electrons of TiO_2 are excited to the conduction band (CB), and then are immediately transferred to MoS_2 through the intimate interfacial contacts for H_2 evolution. As we well know, vertically standing MoS_2 sheets can not only maximally expose active sites for effective HER but also form “superaerophobic” surface which is conducive to reduce gas bubble adhesion for offering constant working area [35]. Additionally, besides the role of cocatalyst, nanoscale MoS_2 itself is highly active for H_2 evolution as a result of the quantum-confinement effect [36]. The H_2 productions on $\text{TiO}_2@\text{MoS}_2$ heterostructures under visible light illumination highlight the effect. In short, the unique heterostructure of $\text{TiO}_2@\text{MoS}_2$ results in the high photocatalytic H_2 evolution.

The recoverability is an important consideration for its practical application of a photocatalyst. The photocatalytic activity stability of $\text{TiO}_2@\text{MoS}_2$ was evaluated by recycling the photocatalyst toward hydrogen evolution reaction. After six recycles lasting 30 h, the H_2 production rates remain highly stable under UV–vis or visible light irradiation (Fig. 10c or d). Thus it can be seen that the $\text{TiO}_2@\text{MoS}_2$ heterostructure is a high-performance photocatalyst for photocatalytic hydrogen production.

4. Conclusions

In summary, a novel $\text{TiO}_2@\text{MoS}_2$ heterostructure with vertically standing single or few-layered MoS_2 nanosheets on porous TiO_2 nanofibers was successfully fabricated via a simple hydrothermal reaction. The $\text{TiO}_2@\text{MoS}_2$ heterostructure exhibits high photocatalytic H_2 production activity with a rate as high as $1.68 \text{ mmol h}^{-1} \text{ g}^{-1}$. As far as we know, it is one of the best photocatalytic HER performances for MoS_2 . The unique structure of the photocatalyst offers a perfect situation regarding the key parameters that determine HER performance. The outstanding recycling HER performance and longevity on the photocatalyst make it promising candidate in practical applications. The present work gives a new insight into engineering novel hierarchical MoS_2 -based heterostructure for efficiently photocatalytic HER.

Acknowledgements

This work was supported by Hunan Provincial Natural Science

Foundation of China (14JJ1015), the National Natural Science Foundation of China (51178173, 51238002, 51272099, 51378187, and 51478171), Program for Innovation Research Team in University (IRT1238), and Program for New Century Excellent Talents in University (NCET-11-0126).

References

- [1] J.J. Cha, K.J. Koski, K.C.Y. Huang, K.X. Wang, W. Luo, D. Kong, Z. Yu, S. Fan, M.L. Brongersma, Y. Cui, *Nano Lett.* 13 (2013) 5913–5918.
- [2] K. Wang, J. Wang, J. Fan, M. Lotya, A. O'Neill, D. Fox, Y. Feng, X. Zhang, B. Jiang, Q. Zhao, H. Zhang, J.N. Coleman, L. Zhang, W.J. Blau, *ACS Nano* 7 (2013) 9260–9267.
- [3] Y. Li, Y. Rao, K.F. Mak, Y. You, S. Wang, C.R. Dean, T.F. Heinz, *Nano Lett.* 13 (2013) 3329–3333.
- [4] R. Prins, V.H.J. Debeer, G.A. Somorjai, *Catal. Rev. Sci. Eng.* 31 (1989) 1–41.
- [5] M. Salmeron, G.A. Somorjai, A. Wold, R. Chianelli, K.S. Liang, *Chem. Phys. Lett.* 90 (1982) 105–107.
- [6] S.M. Ahmed, H. Gerischer, *Electrochim. Acta* 24 (1979) 705–711.
- [7] Q. Zhu, S.L. Wegener, C. Xie, O. Uche, M. Neurock, T.J. Marks, *Nat. Chem.* 5 (2012) 104–109.
- [8] B. Hinnemann, P.G. Moses, J. Bonde, K.P. Jørgensen, J.H. Nielsen, S. Hørch, I. Chorkendorff, J.K. Nørskov, *J. Am. Chem. Soc.* 127 (2005) 5308–5309.
- [9] T.F. Jaramillo, K.P. Jørgensen, J. Bonde, J.H. Nielsen, S. Hørch, I. Chorkendorff, *Science* 317 (2007) 100–102.
- [10] J. Xie, J. Zhang, S. Li, F. Grote, X. Zhang, H. Zhang, R. Wang, Y. Lei, B. Pan, Y. Xie, *J. Am. Chem. Soc.* 135 (2013) 17881–17888.
- [11] H. Wang, D. Kong, P. Johanes, J.J. Cha, G. Zheng, K. Yan, N. Liu, Y. Cui, *Nano Lett.* 13 (2013) 3426–3433.
- [12] Z. Lu, H. Zhang, W. Zhu, X. Yu, Y. Kuang, Z. Chang, X. Lei, X. Sun, *Chem. Commun.* 49 (2013) 7516–7518.
- [13] Y. Li, H. Wang, L. Xie, Y. Liang, G. Hong, H.J. Dai, *J. Am. Chem. Soc.* 133 (2011) 7296–7299.
- [14] Q. Xiang, J. Yu, M. Jaroniec, *J. Am. Chem. Soc.* 134 (2012) 6575–6578.
- [15] D. Kong, H. Wang, J.J. Cha, M. Pasta, K.J. Koski, J. Yao, Y. Cui, *Nano Lett.* 13 (2013) 1341–1347.
- [16] W. Jaegermann, H. Tributsch, *Prog. Surf. Sci.* 29 (1988) 1–167.
- [17] A.B. Laursen, S. Kegnæs, S. Dahl, I. Chorkendorff, *Energy Environ. Sci.* 5 (2012) 5577–5591.
- [18] M. Remskar, A. Mrzel, Z. Skrabar, A. Jesih, M. Ceh, J. Demsar, P. Stadelmann, F. Levy, D. Mihailovic, *Science* 292 (2001) 479–481.
- [19] Y. Tian, J. Zhao, W. Fu, Y. Liu, Y. Zhu, Z. Wang, *Mater. Lett.* 59 (2005) 3452–3455.
- [20] G. Nagaraju, C. Tharamani, G. Chandrappa, J. Livage, *Nanoscale Res. Lett.* 2 (2007) 461–468.
- [21] T.S. Li, G.L. Galli, *J. Phys. Chem. C* 111 (2007) 16192–16196.
- [22] Y. Shi, J.K. Huang, L. Jin, Y. Hsu, S.F. Yu, L.J. Li, H.Y. Yang, *Sci. Rep.* 3 (2013), 1839–1839.
- [23] J. Brivio, D.T. Alexander, A. Kis, *Nano Lett.* 11 (2011) 5148–5153.
- [24] S. Tongay, H. Sahin, C. Ko, A. Luce, W. Fan, K. Liu, J. Zhou, Y. Huang, C. Ho, J. Yan, D.F. Ogletree, S. Aloni, J. Ji, S. Li, J. Li, F.M. Peeters, J. Wu, *Nat. Commun.* (2014), <http://dx.doi.org/10.1038/ncomms4252>.
- [25] D.S. Kong, H. Wang, J.J. Cha, M. Pasta, K.J. Koski, J. Yao, Y. Cui, *Nano Lett.* 13 (2013) 1341–1347.
- [26] J. Zheng, H. Zhang, S. Dong, Y. Liu, C. Tai Nai, H. Suk Shin, H. Young Jeong, B. Liu, K. Ping Loh, *Nat. Commun.* (2014), <http://dx.doi.org/10.1038/ncomms3995>.
- [27] W. Ho, J.C. Yu, J. Lin, J.G. Yu, P.S. Li, *Langmuir* 20 (2004) 5865–5869.
- [28] J.M. Martin, C. Grossiord, K. Varlot, B. Vacher, J. Igarashi, *Tribol. Lett.* 8 (2000) 193–201.
- [29] M. Weber, M. Dignam, *Int. J. Hydrogen Energy* 11 (1986) 225–232.
- [30] K. Tennakone, S. Pushpa, *J. Chem. Soc. Chem. Commun.* 20 (1985) 1435–1437.
- [31] J.Z. Ou, A.F. Chirimes, Y. Wang, S.Y. Tang, M.S. Strano, K. Kalantar-Zadeh, *Nano Lett.* 14 (2014) 857–863.
- [32] E.S. Kadantsev, P. Hawrylak, *Solid State Commun.* 152 (2012) 909–913.
- [33] W. Zhou, Z. Yin, Y. Du, X. Huang, Z. Zeng, Z. Fan, H. Liu, J. Wang, H. Zhang, *Small* 9 (2013) 140–147.
- [34] Y. Hou, Z.H. Wen, S.M. Cui, X.R. Guo, J.H. Chen, *Adv. Mater.* 25 (2013) 6291–6297.
- [35] Z. Lu, W. Zhu, X. Yu, H. Zhang, Y. Li, X.M. Sun, X. Wang, H. Wang, J. Wang, J. Luo, X.D. Lei, L. Jiang, *Adv. Mater.* 26 (2014) 2683–2687.
- [36] S. Linic, P. Christopher, D.B. Ingram, *Nat. Mater.* 10 (2011) 911–921.